Molecular Therapy
Methods & Clinical Development
Original Article

A novel approach to quantitate biodistribution and transduction of adeno-associated virus gene therapy using radiolabeled AAV vectors in mice

Hongzhi Wang,[1] Ran Li,[1] Shraddha Sadekar,[1] Amrita V. Kamath,[1] and Ben-Quan Shen[1]

[1]Preclinical and Translational Pharmacokinetics and Pharmacodynamics, Genentech Inc, 1 DNA Way, South San Francisco, CA 94080, USA

An understanding of recombinant adeno-associated virus (AAV) biodistribution profiles is an important element of a preclinical development program. Here, we have developed a radiolabeling strategy utilizing the co-delivery of ^{125}I (non-residualizing) and ^{111}In (residualizing) radionuclide-conjugated AAVs to provide a detailed distribution quantification at tissue level delineating between the cellular internalized AAV (degraded, ^{111}In-^{125}I) and AAV remaining in the extracellular matrix (intact, ^{125}I). This labeling method has been successfully applied to AAV9 and AAV-PHP.eB as tool molecules without altering the physical properties and biological activities of the AAVs. Upon labeling with either of the radioactive probes, these molecules were systemically injected into C57BL/6 mice. The biodistribution results indicate that AAVs, with a fast distribution profile, were mainly located in the extracellular matrix of highly perfused organs such as liver and spleen at early time points, leading to a difference between capsid quantification and vector genome quantification. The results suggest that the ^{125}I-AAV/^{111}In-AAV co-delivery approach offers a robust and efficient analytical strategy to investigate the detailed tissue distribution of AAV vectors, including both vector genome and protein capsids. This novel method has the potential to be applied to capsid optimization, selection, and lead candidate development.

INTRODUCTION

Adeno-associated virus (AAV) vectors have been developed as a primary gene therapy delivery platform for treatments across diverse therapeutic areas. Originally identified in 1965,[1] the first human AAV was characterized as a replication-deficient virus containing a linear single-stranded DNA genome of approximately 4.7 kilobases encapsulated by a non-enveloped capsid of approximately 25 nm.[2–4] To date, 13 wild-type AAV serotypes have been identified,[5,6] each of which exhibits unique tissue and organ tropism across various animal species.[7–9] Realizing the potential utility as a delivery platform, recombinant AAV vectors were conceived by replacing the wild-type AAV genome with a target gene expression cassette, facilitating its function as a non-replicating carrier for intracellular cargo delivery and episomal DNA persistence within the nucleus.[10,11] Compared with other viral- and non-viral-based gene therapy delivery platforms, AAVs have various advantages including a favorable biosafety profile as recombinant AAV vectors fall into the classification of "non-integrating" vectors, versatile infectivity of both dividing and quiescent cells with various serotypes, and also low immunogenicity, which may assist with more sustained expression in the targeted cells. Currently, a total of 6 AAV therapies have been actively marketed along with more than 200 ongoing clinical trials in various therapeutic areas,[12] and numerous novel AAV modalities are under extensive exploration. The high demand for AAV therapies emphasizes the importance of expediting preclinical and clinical development for AAV-based gene therapies to bring new treatment possibilities to patients.

Elucidating the biodistribution profiles of different components of gene therapy products post *in vivo* administration is pivotal for preclinical development. Information on the biodistribution of recombinant AAV vectors is essential for prediction and assessment of their efficacy and toxicity profiles in nonclinical and clinical studies,[13] providing guidance on the administration route selection and human dose prediction.[14,15] With tremendous efforts being made on capsid engineering to enhance tissue-specific tropism and transduction efficiency,[16] the biodistribution assessment could also assist in novel capsid selection and optimization. However, owing to the multiple components of AAV vectors facilitating their complicated mechanism of action, evaluating biodistribution of viral genome, protein capsid, and transgene product is challenging.[17] Although the AAV capsid is an essential component that is involved in cell binding, internalization,[18] and trafficking[19] within the targeted cell,[20] current biodistribution studies leverage vector genome for pharmacokinetic (PK) analysis of AAVs due to the lack of reliable methodology for viral capsid quantification in tissues. Direct extraction and quantification of capsid proteins such as ELISA is not applicable as the viral proteins are dissociated and degraded after internalization. Fluorophores have been used to tag the capsid to facilitate *in vitro* and *in vivo* imaging analysis.[21,22] Fluorescence-labeled capsid can be tracked via fluorescence microscopy at the

Received 21 March 2024; accepted 15 August 2024;
https://doi.org/10.1016/j.omtm.2024.101326.

Correspondence: Ben-Quan Shen, Preclinical and Translational Pharmacokinetics and Pharmacodynamics, Genentech Inc, 1 DNA Way, South San Francisco, CA 94080, USA.
E-mail: bqshen@gene.com

subcellular level, enabling the elucidation of cell entry and cellular trafficking mechanisms. However, despite the extensive application of fluorophore tracers in *in vitro* studies to investigate AAV biology, *in vivo* fluorescence imaging remains as a semi-quantitative method in *in vivo* studies due to its auto-fluorescence and quenching effects observed in tissue and organs. In comparison, radioisotopes are ideal tracers with high sensitivity for preclinical and clinical *in vivo* imaging and have been applied to AAV capsid modification.[23–25] Limitations remain as the tracers fall short of distinguishing the AAVs that have been transduced into the cell from the vectors remaining in the extracellular matrix since the current AAV biodistribution studies mainly utilize whole tissue homogenates. Researchers using histological microscopy analysis have shown that the majority of AAVs are in interstitial spaces at early time points with a relatively smaller portion of AAVs taken up into the cell,[26] which is in contrast to *in vivo* vector genome biodistribution studies that show a fast distribution of AAV vectors. Such inconsistencies may lead to inaccurate PK/PD (pharmacodynamics) prediction, as the fast-distributed AAV vector genome is not correlated with the high AAV transduction, resulting in the overestimation of the PD effect based on the biodistribution result.

In this context, here we report a novel ^{125}I-AAV/^{111}In-AAV co-delivery strategy, conjugating either ^{125}I (non-residualizing) or ^{111}In (residualizing) radionuclides to the capsid, offering a detailed insight into the AAV biodistribution profile. The ^{111}In radionuclides elucidate tissue-level capsid distribution, while comparing both isotopes enables a detailed distribution quantification at the tissue level delineating between the cellular internalized AAV (degraded capsid, ^{111}In-^{125}I) and AAV remaining in the extracellular matrix (intact capsid, ^{125}I). Complemented with DNA quantification, the study provides a comprehensive biodistribution profile of tool AAV vectors. Dual isotope readings further reveal that AAV particles were mainly located in the extracellular matrix of organs of the reticuloendothelial system such as liver and spleen at early time points (within 3 days post administration). The ^{125}I-AAV/^{111}In-AAV co-delivery strategy can be used as an efficient tool to elucidate a complete AAV distribution profile that facilitates novel capsid optimization and lead candidate selection. The early stage AAV biodistribution kinetics and cellular internalization analysis provide useful data for PK/PD correlation and PK model development. The labeling strategy also has the potential to be combined with single-photon emission computed tomography (SPECT) imaging, providing a noninvasive imaging method for preclinical PK studies.[27,28]

RESULTS

^{125}I-AAV/^{111}In-AAV co-delivery method quantify *in vivo* AAV biodistribution and internalization

Dual-isotope-labeling approaches have been used to investigate antibody internalization and catabolism.[29,30] Here, we utilized a similar methodology to scrutinize and quantify the cellular internalization of AAVs in biodistribution assessments. Ideally, the radioisotope-conjugated AAV vectors should retain the same physical and biological properties as their wild-type AAV particle counterparts. Upon intravenous (i.v.) administration, AAV vectors are distributed to various organs, with some of the AAVs undergoing cellular uptake via transduction as shown in Figure 1. The internalized ^{125}I/^{111}In-AAV capsid undergoes dissociation and degradation and releases both ^{125}I- and ^{111}In-DOTA-containing catabolites. While the most likely ^{125}I-containing catabolite, ^{125}I-iodotyrosine, is rapidly effluxed from the cell and eliminated through urine excretion, ^{111}In-DOTA-containing catabolites (often ^{111}In-DOTA-lysine in the case of labeled proteins) are trapped in cells given the impermeability of charged/polar radio-metal chelate through the cell membrane. By counting ^{125}I and ^{111}In individually, ^{125}I represents the intact AAV vectors mainly located in the extracellular matrix, while ^{111}In reveals the total AAV vectors accumulated in the tissue, including both intact AAVs remaining in interstitial spaces and dissociated AAV vectors already transduced into the cells. The difference between ^{125}I and ^{111}In radioactivity levels, derived from the degradation of capsids, elucidates the cellular uptake of AAV vectors.

Radioisotope conjugation of AAV capsids with high radioactive specificity

The AAV capsid was orthogonally labeled with two distinct radioisotopes via specific chemical conjugation techniques. The non-residualizing isotope, ^{125}I, was directly conjugated to tyrosine residues, while the residualizing isotope, ^{111}In, was chelated to a DOTA group that was initially conjugated to the capsid using TFP ester reaction with primary amine groups (Figure 2A).

To achieve ^{125}I labeling, the Iodogen method was used to oxidize iodide to a reactive species (I^+), which directly conjugates to the capsid.[31] To avoid direct exposure of the capsid to harsh oxidative conditions, sodium ^{125}iiodide solution was first incubated with Iodogen and then the activated ^{125}I solution was transferred to a separate tube containing the AAV (2×10^{12} vector genomes [vg] in 100 μL phosphate-buffered saline [PBS] buffer) for the labeling reaction. The reaction was stopped by transferring the mixture to a desalting column, where ^{125}I-AAV was purified into PBS buffer.

Chelating agents such as DOTA or NOTA were frequently utilized to chelate radioactive isotopes, such as ^{111}In, onto AAV. In this study, we used DOTA-dPEG$_4$-TFP ester linker to first conjugate the DOTA to capsid via TFP ester chemistry.[32] Similar to the NHS ester reaction, TFP esters targeted primary amines on the biomolecules, thus attaching the DOTA group to the capsid protein. Advantageously, TFP esters display enhanced stability at basic pH, considerably outpacing succinimidyl esters. The DOTA-dPEG4-TFP was incubated with AAV capsid (2×10^{12} vg in 100 μL PBS buffer) at 4°C overnight, following by buffer exchange to ammonium acetate buffer (pH 7.0) to remove unbound linkers and facilitate the ^{111}In chelation process. After incubating with ^{111}In at 37°C for 45 min, the reaction was stopped via adding EDTA to chelate non-labeled ^{111}In, and subsequently purified using a desalting column.

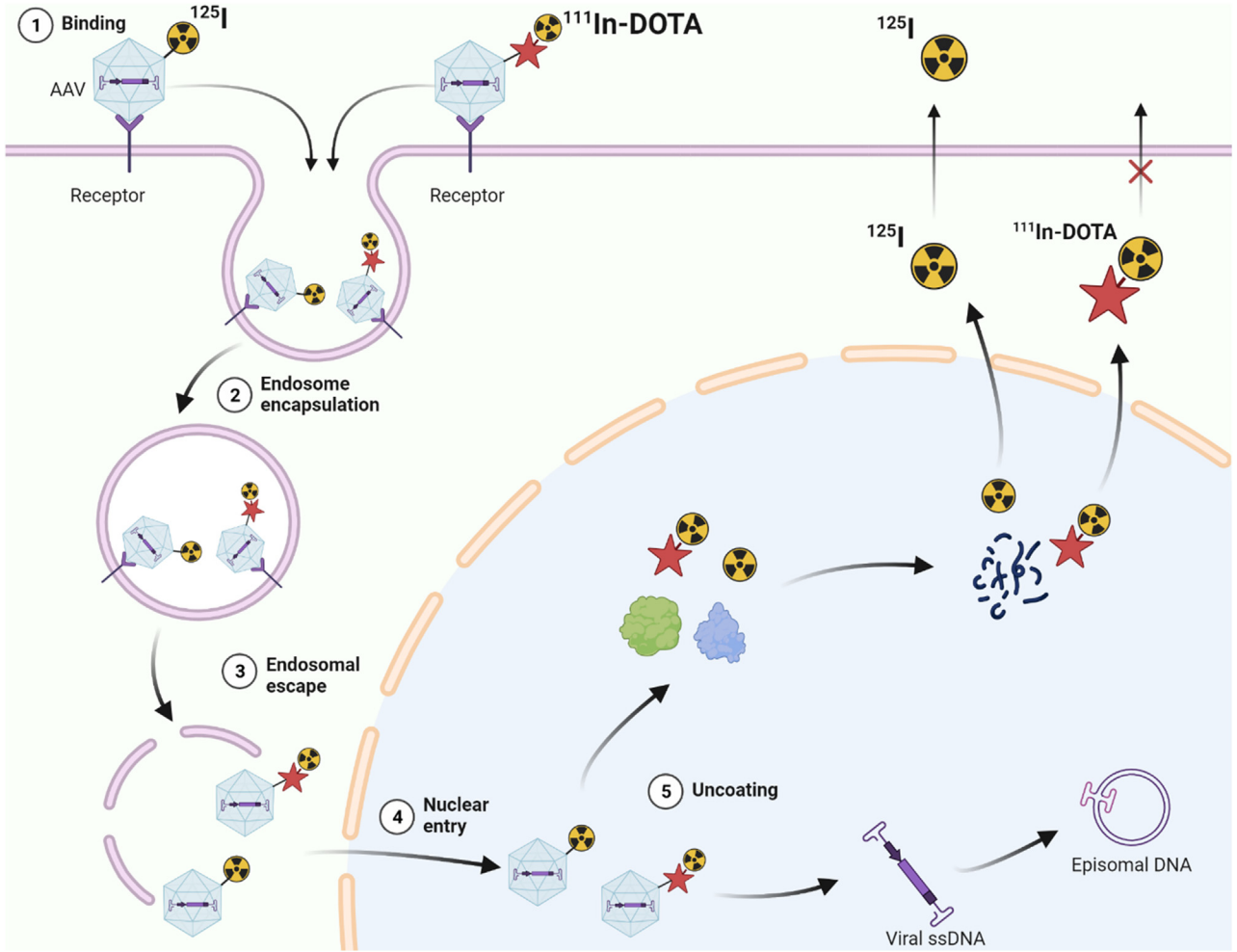

Figure 1. Schematic diagram of the cellular processing of radiolabeled AAV

Both ^{125}I- and ^{111}In-DOTA-labeled AAVs enter the cell by receptor-mediated endocytosis. Following their release from endosomes, a portion of AAV vectors are intracellularly trafficked to the nucleus, uncoated, and the AAV genome is released. The AAV single-stranded DNA genome is then converted into double-stranded episomal DNA, followed by transcription and translation for the expression of the transgene product. The dissociated capsid proceeds to degradation. The polar ^{111}In-DOTA-modified catabolites are trapped in the cell due to the polarity. In contrast, iodinated catabolites are rapidly effluxed from cells.

The labeled vectors were further concentrated using a 5 kDa cutoff centrifugal filter to a stock concentration of $\sim 1 \times 10^{13}$ vg/mL for the following studies.

AAV capsid integrity remains intact with isotope conjugation

Throughout the labeling process, we deliberately avoided using low pH condition and minimized the reaction duration. Nevertheless, the AAV capsid was incubated in a range of buffer pH values to enhance the conjugation chemistry, which might damage the integrity of AAV vectors. In addition, the high energy reactive [I^+] species have the potential to break the chemical bond. To assess any potential damage to the AAV capsid's structural integrity resulting from the labeling process, we characterize the size and purity of labeled AAV capsid via dynamic light scattering (DLS) and size-exclusion chromatography-high-performance liquid chromatography (SEC-HPLC). AAV9 and AAV-PHP.eB are shown as representative examples.

AAV capsids are approximately 25 nm diameter solid spheres under TEM imaging. The DLS measurement indicates the hydrodynamic radius of both wild-type AAV9 and AAV-PHP.eB as around 15 nm (15.6 and 15.8 nm, respectively). Radioisotope-labeled AAV capsids did not exhibit significant size changes; however, large particles (100 nm) were observed, indicating the existence of capsid aggregation (Figure 2B). Based on the DLS measurement, more than 98% of AAV capsids remained intact.

Further examination of potential damage of capsid proteins, for example, protein cleavage, during conjugation was undertaken using western blot, which enabled the visualization of the three viral

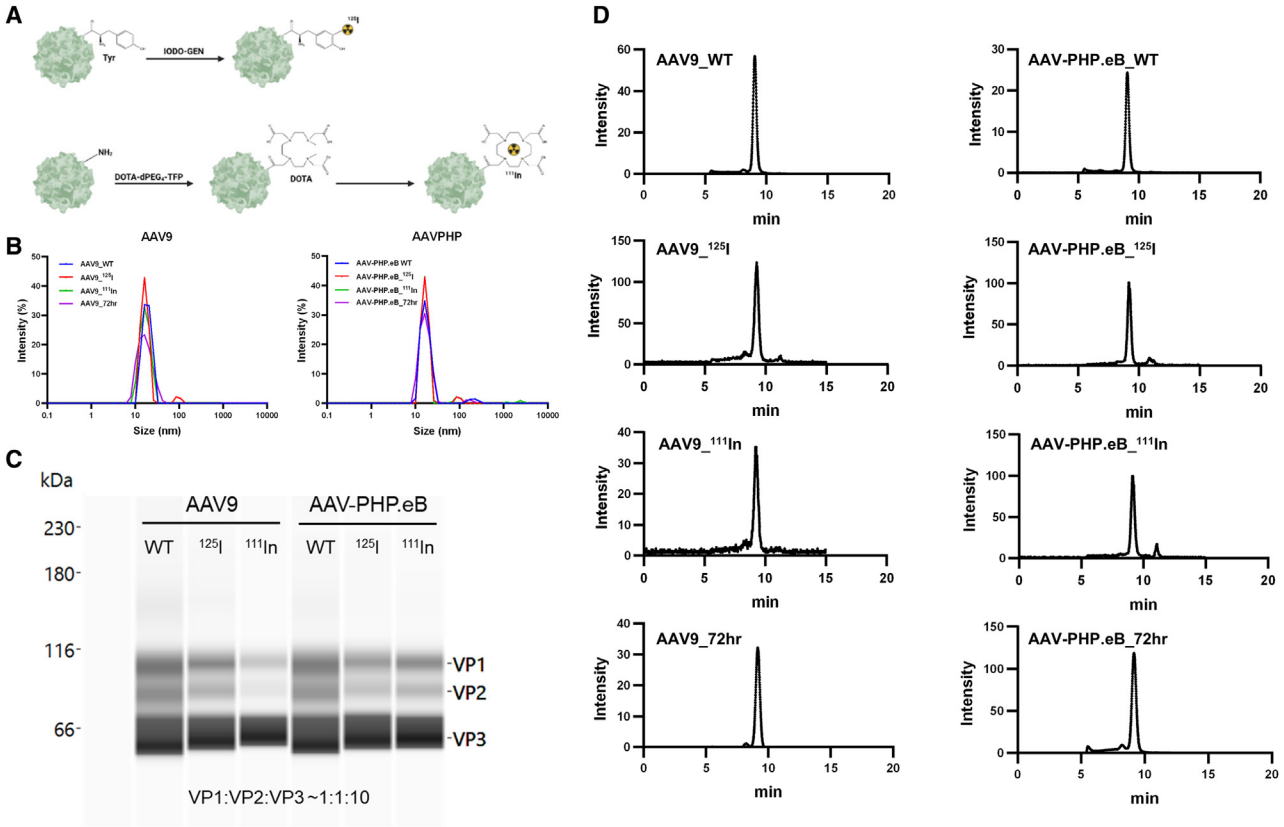

Figure 2. Synthesis and characterization of radiolabeled AAV vectors

(A) Synthesis of radiolabeled AAV vectors. ^{125}I was directly conjugated to tyrosyl residue by electrophilic substitution reaction on the aromatic moiety. DOTA groups that were initially introduced by TFP ester conjugation to primary amines on the capsid, followed by ^{111}In chelation into the AAV-DOTA complex. (B) Size distribution of unlabeled AAV vectors (blue), ^{125}I -AAVs (red), ^{111}In -AAVs (green), and radiolabeled AAV mixtures incubated in PBS buffer after 72 h (purple). (C) Capillary electrophoresis of AAV9 vectors (unlabeled AAV, ^{125}I labeled, and ^{111}In labeled) and AAV-PHP.eB vectors (unlabeled AAV, ^{125}I labeled, and ^{111}In labeled), respectively. The three bands depict VP1, VP2, and VP3. (D) HPLC profiles of the AAV9 and AAV-PHP.eB reaction mixture and purity analysis. Unlabeled AAV vectors were detected using 280 nm channel as size control. Purity analysis of radiolabeled AAVs (^{125}I -AAV, ^{111}In-AAV, and AAV mixture incubated after 72 h) was examined by radio-HPLC.

proteins (VP1, VP2, and VP3). The radiolabeled AAV capsid showed slightly higher protein bands than unlabeled AAVs due to increased molecular mass from the conjugation of ^{111}In/DOTA groups to the viral proteins (Figure 2C). The consistent protein abundance ratios, maintained at 1:1:10 for VP1, VP2, and VP3, affirms that the capsid proteins remain unaffected after conjugation.

Determination of purity and stability of radiolabeled AAV vectors

To assess the radiochemical purities of labeled AAV capsids, the labeled products were subjected to SEC-HPLC for purity analysis, where capsid protein and radioisotope were simultaneously monitored in separate channels (Figure 2D). One predominant peak eluted at the same time (9.5 min) in both detection channels, suggesting the successful conjugation of radio probes to the capsid proteins, without significantly altering the size of AAV capsids. A minor peak eluting at 11 min represents the unconjugated isotope remaining in the product. Calculating based on the peak area in the radiation channel, the radiochemical purity of ^{125}I and ^{111}In both exceeded 98%.

Although all AAV particles used for *in vitro* and *in vivo* studies are freshly labeled to ensure high radioactivity, we evaluated the AAV capsid and radioisotope label stability in PBS buffer to identify any nonspecific binding of radioisotope to the capsids, which would compromise the quantification accuracy. After incubation in PBS at room temperature for 72 h, both DLS and HPLC data remained the same as the stock sample (Figures 2B and 2D). The hydrodynamic radius persisted at around 15 nm, with no significant aggregation observed. Absence of free radioactive peaks in the HPLC analysis further validated the stability of the covalent radioisotope conjugation.

Titration and characterization of radiolabeled AAV vectors

Following the confirmation of successful radio probe labeling to AAV vectors, we proceeded to quantify the AAV genome and capsid titration to calculate the full/empty ratio and isotope number of AAV labels. Genome titers were determined using digital PCR and capsid titers were measured via ELISA, which can only detect intact capsid. Comparative analysis between stocked and labeled AAV

vectors demonstrated comparable full/empty ratios for both AAV9 (79.30%) and AAV-PHP.eB (78.50%). The number of isotope labels per capsid was calculated based on the initial isotope specific activity, AAV capsid titer, and product radioactivity with decay correction. The Iodogen method yielded an average of 11.21 ^{125}I atoms per AAV9 capsid and 9.81 ^{125}I per AAV-PHP.eB capsid, while ^{111}In DOTA chelation gave 4.2 and 3.8 ^{111}In radionuclides of each AAV9 and AAV-PHP.eB capsid, respectively.

In vitro uptake and transduction analysis of AAV

With the confirmation that the radioisotope labeling did not compromise the biophysical attributes of AAV vectors, we further employed *in vitro* studies to examine whether the capsid conjugation maintained the biological activity of AAVs. For analyzing the cellular uptake and transduction efficiency, we used AAV vectors that encode green fluorescent protein (GFP) from the CMV promoter, where GFP can be easily quantified through fluorescence microscopy and cytometry.

To evaluate potential impacts of radiolabeling chemistry on biological activity, the infectious titers of both labeled and unlabeled AAV2 and AAV9 were assessed at a multiplicity of infection (MOI) from 100,000:1 to 1:1 in both HEK293T cells and HUVEC lines, respectively. Quantification of GFP-expressing cells after a 2-day infection indicated no changes in infectious titer between labeled and unlabeled AAVs across both cell lines. Further analysis of transduced genome copies (GCs) and fluorescent microscopy images further confirmed the comparable transduction efficiency between labeled and wild-type AAVs (Figure 3A). In addition, AAV2 showed a higher *in vitro* transduction efficiency than AAV9, which is consistent with previous publications.

To assess the versatility of radioisotope labeling as a generalized approach without serotype specificity, we labeled a total of 8 AAV serotypes using the previously described method for subsequent experiments. Both HEK293T cells and HUVECs were infected at a constant MOI of 1,000 vg/cell and analyzed for GFP expression 2 days post infection. Compared with unlabeled AAVs, the GFP-positive rate of labeled AAV across all serotype-treated cells remained the same in both HEK293T cells and HUVECs (Figure 3B). Variances in AAV uptake among serotypes can be attributed to inherent differences in *in vitro* transduction efficiency.[33]

To examine whether our ^{125}I-AAV/^{111}In-AAV co-delivery method could provide insights into AAV cellular uptake, three treatment groups including AAV2, AAV2-Y444F (A site-directed mutated AAV2 with increased transduction efficiency), and AAV2 with anti-AAVR (blocking cell surface AAVR to inhibit AAV cell entry) were incubated with HEK293T cells at 1,000 vg/cell for 72 h to explore the correlation between DNA quantification and cell internalization as measured by ^{111}In-^{125}I (Figure 3C). Given the previous result that isotope-labeled AAV retained comparable activity as unlabeled AAV vectors, in this study we mixed stock AAV with ^{125}I-AAV and ^{111}In-AAV, respectively, to generate AAV mixture with tracer amount of radioactivity (~100,000 dpm/5 × 10^8 vg AAV particles). In general, both DNA concentration and radioactivity derived from ^{125}I and ^{111}In revealed similar trends at 24 h after treatment, indicating capsid uptake with minimum dissociation. Over 24 h, the ^{125}I signal decreased while the ^{111}In signal remained aligned with qPCR results, suggesting that, upon cellular uptake and subsequent dissociation, cleaved ^{125}I was released into the medium while ^{111}In-DOTA was retained in the cell. Comparing among groups, AAV2-Y444F showed an overall higher cellular uptake than wild-type AAV2 in terms of both genome quantification and cell internalization as measured by radioactivity. Whereas anti-AAVR treatment inhibited receptor binding and endocytosis, leading to lower cell entry than the untreated AAV2 group as indicated by both qPCR analysis and radioactivity measurement.

To further validate the observed AAV cellular uptake results, we labeled the AAV2 vectors with anti-AAV2 antibody that specifically recognizes intact AAV capsids, alongside nuclei staining with DraQ5 dye, followed by confocal microscopy imaging (Figure 3D). The confocal fluorescence images further confirmed the previous result. AAV2 showed increased cellular uptake during the first 24 h, as reflected by the increased fluorescence intensity of intact capsids. Subsequent reduction in fluorescence signal after 24 h indicated gradual dissociation of capsids. A similar result was observed in the other two groups with overall higher fluorescence intensity in the AAV2-Y444F treatment group and significant lower fluorescence in the anti-AAVR-treated group. These result affirm the effectiveness of dual isotope co-delivery approach on AAV cell internalization analysis.

In vivo biodistribution study of AAV

The tissue biodistribution of ^{125}I/^{111}In radioisotope-labeled AAV9 and AAV-PHP.eB were evaluated in C57BL/6 mice. This mouse strain was selected because previous studies have shown significant brain accumulation of AAV-PHP.eB following i.v. administration in C57BL/6 mice, in contrast to AAV9, which exhibited negligible brain uptake.[34] Unlabeled AAV, ^{125}I AAV, and ^{111}In AAV were freshly prepared and mixed proportionally to achieve an administration dose comprising 10 μCi of ^{111}In, 10 μCi of ^{125}I, and 1 × 10^{12} vg per mouse (Table 1). Following a single dose i.v. administration, blood and tissue samples were harvested at designed time point (n = 4). Levels of ^{125}I and ^{111}In were quantified simultaneously under separate energy windows (15–85 keV for ^{125}I, 237–257 keV for ^{111}In), while DNA was extracted and quantified via qPCR.

The blood PK profiles were derived from both radioactivity (%ID/mL) and qPCR (GFP copy/mL), both normalized to blood volume. Overall, the radioactivity results (Figure 4A) align with the DNA quantification results (Figure 4B). A rapid decline in blood concentration was observed within the initial 3 days, suggesting fast AAV distribution *in vivo*. The ^{125}I radioactivity was slightly elevated compared with the ^{111}In readout, likely due to efflux of the free ^{125}I removed from degraded capsids.[35] Compared with AAV9, AAV-PHP.eB exhibited a faster clearance because of higher tissue accumulation, with particularly significant brain uptake. The

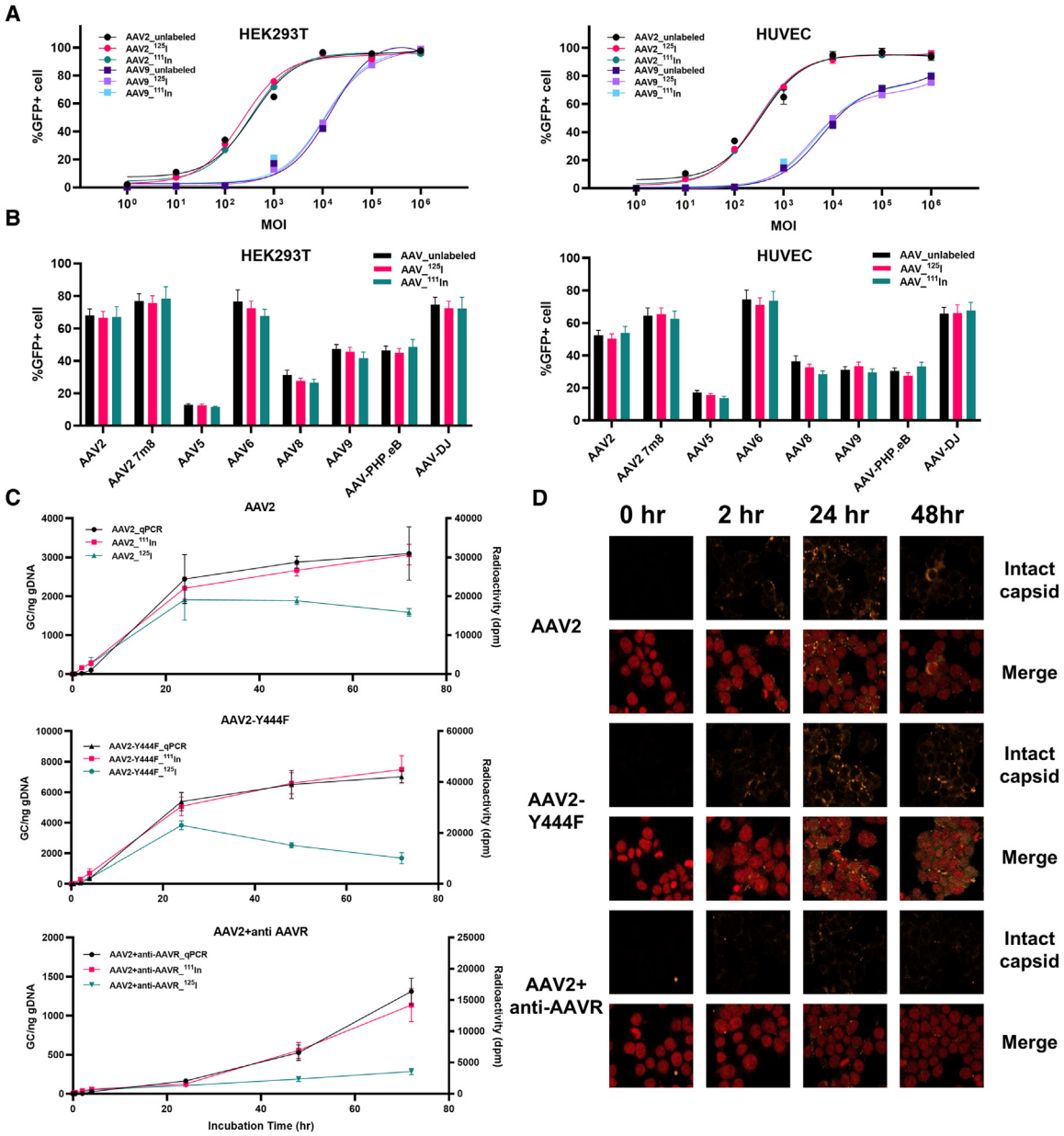

Figure 3. *In vitro* transduction efficiency of radiolabeled AAVs

(A) Quantification of the GFP-positive cell percentage of unlabeled AAV, ^{125}I-AAV, and ^{111}In-AAV of HEK293T cells (left) and HUVECs (right) at MOI ranging from 100,000 to 1 vg/cell. (B) Quantification of GFP-positive HEK293T cells (left) and HUVECs (right) percentage infected by unlabeled AAV, ^{125}I-AAV, and ^{111}In-AAV. (C) AAV vector genome transduction kinetics measured by radioactivity and qPCR, respectively. The data are represented as the mean ± SD. n = 4 per time point. (D) Confocal fluorescence microscopy images HEK293T cells after infection with AAV2, AAV2-Y444F, and AAV2 with anti-AAVR inhibition (cell nuclei stained with DraQ5 appear in red, and intact AAV particles stained with Alexa Fluor 555 appear in yellow).

radioactivity reached the lower limit of quantification (LLOQ) at 3 days post injection, whereas detectable DNA persisted longer than 5 days.

Tissues and organs were harvested at 4 h, and 1, 3, 7, and 21 days post injection (n = 4). The percentage of injected dose of ^{125}I and ^{111}In per gram of tissue (%ID/g) was measured, respectively, with decay adjustment and normalized to organ weight. Total tissue accumulation (Figure 5A) was derived by radioactivity from ^{111}In only. Similar tissue biodistribution patterns between the two AAV serotypes were observed in major organs. Both AAV serotypes showed distribution within 3 days post injection in highly perfused organs, including the liver, spleen,

Table 1. Titer of AAV mixtures injected into the mouse

	AAV	Dose (10 μCi)	Genome titer (GC/mL)	Capsid titer (particles/mL)	Full/empty ratio (%)
1	^{125}I/^{111}In-AAV9	10^{12} GC	7.28×10^{12}	9.18×10^{12}	79.30
2	^{125}I/^{111}In-AAV-PHP.eB	10^{12} GC	8.25×10^{11}	1.05×10^{12}	78.50

lungs, heart, and kidney (Tables S1 and S2). At 3 days post injection, radio probes remained detectable in spleen and liver, while in other major organs the radioactivity decreased to background level. Besides the similarity of the organ distribution, AAV-PHP.eB exhibited overall higher tissue accumulation, with a remarkable elevated brain penetration. The difference could be contributed to by the high affinity of AAV-PHP.eB to the LY6A receptor, which is highly expressed in brain endothelial cells. Due to the short half-life of ^{111}In (2.8 days), the radiation signal decayed to LLOQ after 7 days.

To further differentiate the AAV localized in the extracellular matrix and those that had been internalized, we have analyzed the difference between the ^{111}In and ^{125}I radio probes post i.v. injection (Figure 5B). A side-by-side comparison of the radioactivity from these two probes in different tissues not only enabled us to monitor the AAV capsid tissue distribution but also helped to evaluate internalization of AAV vectors. In general, the internalized AAV quantification results are consistent with total tissue accumulations in most of the organs (Tables S1 and S2). Heart and muscle are known to be of high specificity of AAV9, which also exhibits high transduction efficiency in the results. However, in high perfusion organs such as liver and spleen, a remarkable distinction was observed between total and internalization results. Specifically, at days 1 and 3, both AAV serotypes demonstrated a high total accumulation in liver (∼30%) and spleen (∼25%), whereas much lower quantification from internalized AAVs indicated that the majority of AAV vectors were located in extracellular matrices of high accumulated organs without being transfected into cells.

To further investigate this observation, we dissociated the harvested organs and washed them with PBS to eliminate extracellular AAVs, followed by qPCR quantification (Figure 5C). The qPCR results further confirmed the substantial brain accumulation of AAV-PHP.eB (∼44,000 GC/μg genomic DNA [gDNA] on day 1). Specific AAV accumulations, in line with previously published AAV9 tissue tropism, were evident in the heart and muscle. Spleen persisted in the highest organ accumulation; however, liver did not exhibit elevated AAV DNA concentration compared with other organs after 3 days (Table S3). The qPCR data were consistent with AAV internalization results quantified by radioactivity measurements, further confirming that AAV vectors are mostly retained in the interstitial space of highly perfused organs. Notably, adipose tissue, such as mammary fat pad and body fat, also showed AAV transduction, which was not investigated in other studies but was consistent with capsid barcode studies.[36]

To evaluate the correlation between qPCR results and radioactivity measurements, biodistribution results at days 1 and 3 were plotted in the same graph (Figure 6). Overall, qPCR results had a better correlation with internalization result than with total capsid distribution (R^2 = 0.64 vs. 0.93, 0.66 vs. 0.87, respectively). These results demonstrated that the spatial distribution of AAV vectors contribute to the different quantification result between two measurement methods.

Transgene product analysis of AAV

To further analyze the biodistribution of AAV vectors, we extracted GFP protein from the harvested organs and measured the transgene product levels. The GFP concentration was measured using ELISA and the result was normalized to total protein level (Figures 7A and 7B). In both AAV-treated groups, GFP protein began to be detectable by day 3 and the expression kept increasing steadily until 21 days. Among harvested organs, heart, muscle, and lung have substantial expression. The AAV-PHP.eB treatment group exhibited elevated brain expression, which is consistent with DNA results. Collectively, quantification of transgene expression confirmed results from the biodistribution studies.

DISCUSSION

An understanding of biodistribution is a crucial aspect of many nonclinical drug development programs. Current methods of AAV distribution assessment rely on measuring the vector genome from organ or tissue homogenate. The quantification result is unable to differentiate intracellularly transduced AAV vectors from those localized within the extracellular matrix, which is important for PK/PD correlation and dose projection. Researchers using histological microscopy analysis have identified that the majority of AAVs is present in in interstitial spaces at early time points, which could not be observed by *in vitro* studies. Such inconsistencies might lead to inaccurate *in vitro-in vivo* correlations as the target organ exposures might not be achieved by projected efficacious doses. Considering the rapid distribution profile of AAV vectors, accurate quantification of early AAV distribution kinetics could provide useful information for PK modeling. As such, a quantitative method that could provide spatial distribution in organs and tissues is needed to gain detailed ADME knowledge of AAV vectors.

Substantial efforts have been made to delineate the location of AAV vectors and monitoring their distribution from organ-level down to subcellular dimensions. Fluorescent imaging applications involving multicolor labeling, dynamic tracking, and super-resolution microscopy have been extensively utilized in AAV research.[37] Given the high resolution and sensitivity of fluorescence microscopy, fluorophore-labeled AAV vectors have been widely used to reveal the dynamics, and subcellular and sub-nuclear localization, of AAV particles.[38–41] The engineering and modification of AAVs have

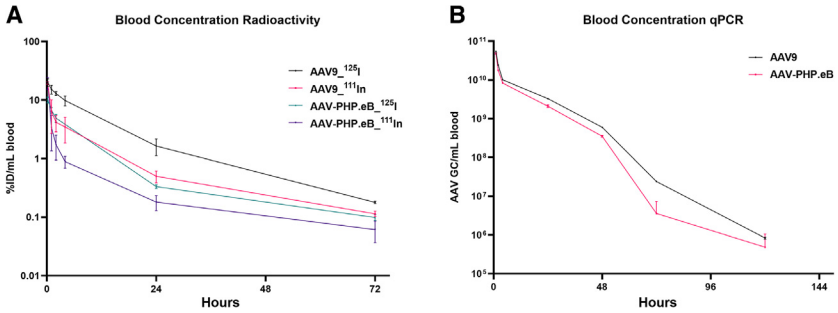

Figure 4. Profiles of blood concentration of radiolabeled AAV9 and AAV-PHP.eB following a single i.v. administration

(A) Radioactivity of dual-isotope-labeled AAV (as a percentage of the injected dose) in plasma in mouse up to 3 days post administration. (B) AAV genome copy of dual-isotope-labeled AAV in plasma in mouse up to 5 days post administration. The data are represented as the mean ± SD. $n = 4$ per time point.

accelerated remarkably by the development of capsid tracking methodologies. Nonetheless, despite advances in fluorescence imaging technologies over recent decades, challenges remain in accurate quantification of the labeled AAV vector biodistribution *in vivo* or *ex vivo* based on fluorescence imaging. The intrinsic hydrophobicity of external fluorophore probes may impact the transduction efficiency and tropism of labeled AAVs. In addition, auto-fluorescence and quenching effects further limit their utility as a semi-quantitative method in *in vivo* assessments. To accelerate the preclinical and clinical development of new therapeutic modalities, a quantitative analytical method, preferably a clinically used technique, is imperatively needed.

In this study, we used two orthogonal radioisotope labeling techniques, conjugating a non-residualizing ^{125}I probe or a residualizing ^{111}In probe to the capsid, to address key questions related to distribution and cell internalization of AAV vectors post systemic injection. Upon AAV vector distribution and internalization, the ^{125}I probes are rapidly excreted, whereas ^{111}In remains intracellularly.

Previous literature documents successful AAV capsid labeling using radioisotopes by direct conjugation[23,42] or DOTA group chelation[25]; however, these methods posed challenges, either affecting the biological activity or necessitating specialized multi-chelators. We have refined the labeling conditions, leveraging commercially available linkers, to ensure high labeling efficiency and radiochemical purity. This optimized method, which avoided extreme pH and temperature exposures, preserved AAV integrity. Notably, the two isotopes were conjugated to the capsid via orthogonal chemistry; however, each capsid was exclusively labeled with one isotope (i.e., mixing individually labeled capsid preparations) for two reasons: (1) it minimizes reaction durations and pH exposures, thereby maintaining AAV integrity, and (2) the unique radioactive specificities of the isotopes allows for precise dose radioactivity when combining ^{125}I-AAV, ^{111}In-AAV, and unlabeled AAV. Characterization including DLS and western blot validated that the physical properties of AAV remained intact, and *in vitro* assessments confirmed that both probes did not alter the transduction efficiency. The radioisotope labeling method has been implemented on a wide range of AAV serotypes and could also be applied to engineered AAV capsids, while the labeling efficiency needs to be further optimized as the capsid surface amino acid might be changed.

In *in vitro* proof-of-concept studies, we applied this dual-isotope-labeled AAV to three treatment groups: AAV2, AAV2-Y444F, and AAV2 with anti-AAVR inhibition to test our hypothesis. AAV2 is well documented for its high *in vitro* transduction efficiency.[33] The AAV2-Y444F variant is derived from AAV2 with a site-directed mutant of surface-exposed tyrosine residues that allow the AAV vectors to evade phosphorylation and subsequent ubiquitination and, thus, significantly enhancing intracellular trafficking and delivery of the viral genome to the nucleus.[43,44] Pre-treatment with anti-AAVR blocked the AAVR on the cell surface, inhibiting AAV2 endocytosis by 10-fold.[45,46] In AAV2-infected cells, vector cellular uptake and accumulation of the AAV vectors were captured by qPCR and ^{111}In radioactivity, where a continuous increase in signal was observed. Meanwhile, the proteasome-mediated degradation of capsids was recorded by both ^{125}I radioactivity and confocal imaging of intact vectors, where the signal decreased after 24 h due to the dissociation and degradation of AAV capsids. Comparative analysis among three treatment groups revealed that Y444F-mutated AAV2 resulted in higher transduction efficiency, whereas cellular uptake was significantly inhibited by anti-AAVR antibodies. These *in vitro* study results validate the capability of the dual isotope co-delivery strategy in AAV cellular uptake analysis.

In this study, we applied a ^{125}I-AAV/^{111}In-AAV co-delivery approach to study an AAV9 serotype and its variant AAV-PHP.eB as tool molecules to assess their biodistribution and cell uptake in the C57BL/6 mouse at early time points. Biodistribution assessments of gene therapy are usually conducted at the end of definitive studies. However, AAV vectors have been reported with a fast *in vivo* distribution profile and rapid transduction rate, thus an understanding of AAV biodistribution kinetics at early time points facilitates the PK/PD correlation and prediction of these therapeutics.

Recent publications reported that AAV-PHP.eB exhibited significant brain accumulation, specifically in C57BL/6 mice, due to a LY6A receptor-mediated pathway, while retaining similar distribution pattern in other organs with AAV9.[47] Analyzing the ^{111}In measurement results, similar biodistribution profiles were also observed in this study. Typical AAV9 tissue tropism to heart and muscle was detected and a high accumulation was found in spleen and liver. The unique brain accumulation was further confirmed. These results aligned well with published data, demonstrating the feasibility of using ^{111}In as

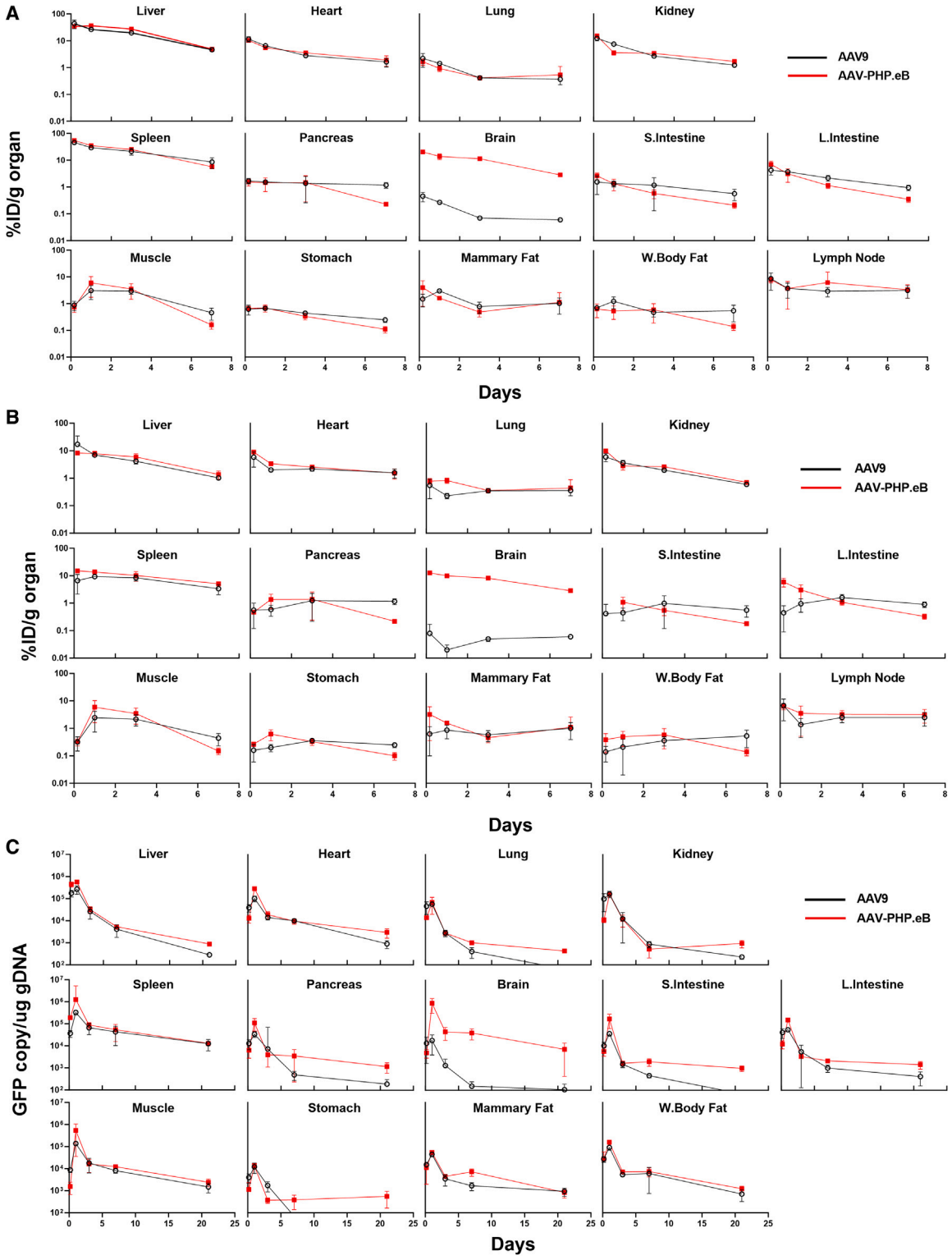

(legend on next page)

a tracer to investigate AAV capsid biodistribution over a long duration.

However, a remarkable distinction was evident when equating qPCR data with total tissue distribution outcomes from ^{111}In-only measurement, particularly in organs with high perfusion like the liver. Significant accumulation was detected in highly perfused organs, whereas qPCR results did not show much difference. Such discrepancies could lead to the failure of dose prediction as the AAV capsid accumulation is not consistent with vector genome level. One hypothesis is that some of the AAV vectors detected in the tissue were not transfected into the cell followed by degradation. To elucidate the difference between various measurements, we conjugated a non-residualizing isotope, ^{125}I, to the AAVs to differentiate the cell-internalized AAV vectors from the capsids remaining within the extracellular matrix. The result suggests significant AAV vector presence in the extracellular matrix in organs such as the liver and spleen without cellular uptake. Compared with the qPCR result, the internalized AAV vector quantifications have a better correlation with the DNA results than with the total tissue accumulation data. The transgene product quantification further confirmed the observation as higher protein concentrations were detected in tissues of higher AAV internalization. The interstitial space accumulation was also observed in previous publications,[26] where highly sensitive ISH assay demonstrated that the majority of AAVs were restricted in the extracellular matrix at early time points.

The implementation of a dual radioisotope co-delivery approach demonstrates its capability to extensively assess the biodistribution and cellular transduction properties of engineered AAVs. However, certain constraints persist in our investigations. Due to the limitations inherent in the resolution of radio detection techniques, the isotope tracers could not be effectively visualized at the cellular scale. As a result, applications of this approach for identifying cell types within organs that contribute to the biodistribution and uptake are restricted. Moreover, fundamental aspects of the AAV life cycle, including cellular entry, endocytosis, intracellular trafficking, and post-entry block, remain inadequately evaluated by the radiolabeling method. It is worth emphasizing that, while the radiolabeling technique enhances our current research techniques, it is not a substitute but rather a supplementary tool to widely used methods such as fluorescence microscopy and flow cytometry. Radioisotope tracers are particularly advantageous for *in vivo* preclinical and clinical investigations; however, the elucidation of AAV biological mechanisms and the precise determination of AAV locations at a subcellular level are still heavily dependent on the advancements in high-resolution imaging techniques and molecular biology research. Consequently, further efforts to integrate diverse methodologies and develop a comprehensive research framework are crucial for accelerating the preclinical development of AAV-based therapeutics.

In summary, we have developed a ^{125}I-AAV/^{111}In-AAV capsid co-delivery approach to quantify *in vivo* biodistribution and transduction of AAV-based gene therapy. This method not only tracks capsid biodistribution but also gains intricate insights into AAV vector spatial distribution in the context of tissue microenvironments. Moreover, this labeling strategy holds promise for integration with SPECT/CT imaging, providing a noninvasive imaging method for preclinical PK studies.

MATERIALS AND METHODS

AAV and cells

All of the AAV serotypes carry CMV and GFP reporters and were at $\sim 2 \times 10^{13}$ vg/mL titration range. AAV used in this studies were purchased from Virovek (Hayward, CA).

The human cell line HEK293T cells (CRL-3216, ATCC, Manassas, VA) were cultured in DMEM medium (Gibco, Waltham, MA) containing 10% FBS (Gibco). HUVECs (C2519A, Lonza, Hayward, CA) were cultured using EGM BulletKit (Lonza). All the cells cultured in flasks were put in a 37°C incubator under 5% CO_2 and a humidified atmosphere.

Radioisotope labeling of AAVs

For ^{125}I radiolabeling, the Iodogen method was used to conjugate ^{125}I directly to the AAV capsid tyrosine group (Figure 2A). In brief, 100 μL 0.1 M PBS (pH ∼7.4) was added to 6 μL NaI solution (∼2 mCi, Revvity, Waltham, MA) to adjust the pH to ∼7.5. The radioiodine solution was transferred to an Iodogen tube (Thermo Scientific, Waltham, MA) and kept in the vial for 6 min at room temperature with intermittent stirring to activate ^{125}I. The reactive ^{125}I solution was then transferred to a 1.5 mL tube containing 1×10^{12} vg of AAVs formulated in 50 μL PBS and kept at room temperature for 5 min with periodic gentle mixing. Following radiolabeling, the product mixture was passed through a NAP-5 size-exclusion column (Cytiva) to remove free ^{125}I and then eluted with 500 mL PBS. Purified ^{125}I-AAV was concentrated using MWCO 50k filter column (Millipore Sigma, Burlington, MA) at 3,000 × *g* for 20 min with two PBS washing cycles and concentrated in an ∼50 μL volume.

For ^{111}In labeling, DOTA-dPEG4-TFP ester (Sigma-Aldrich, St. Louis, MO) was used as the linker to chelate ^{111}In and conjugated to the primary amine group on AAV capsids. In brief, buffer exchange of 1×10^{12} vg of stock AAVs formulated in PBS buffer was conducted using a filter column. The AAVs were re-formulated in 0.1 M PBS buffer solution (pH 7.4), then 0.1 mg DOTA-dPEG4-TFP ester

Figure 5. The tissue concentration-time profiles of radiolabeled AAV9 and AAV-PHP.eB after a single dose via i.v. administration in C57BL/6 mice

(A) The tissue radioactivity from total accumulated AAVs (^{111}In only). (B) The tissue radioactivity from cell internalized AAVs (^{111}In-^{125}I). (C) Tissue distribution of AAV vector genome quantified by qPCR up to 21 days post administration. The data are represented as the mean ± SD. $n = 4$ per time point. S. Intestine, small intestine; L. Intestine, large intestine; B. Marrows, bone marrows; W. Body Fat, white body fat. Concentrations are reported in %ID/mL or %ID/g.

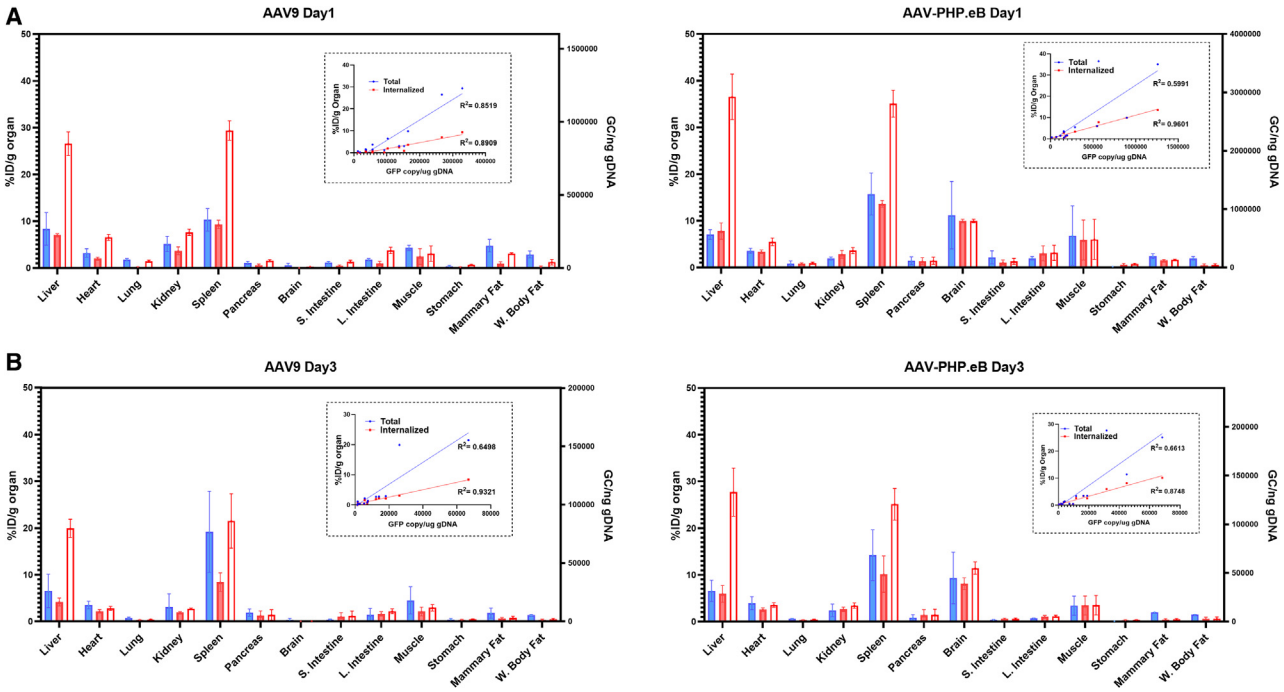

Figure 6. Correlation of tissue distribution analysis by radioactivity vs. qPCR quantification

(A) Comparison of tissue vector genome quantification (right y axis), radioactivity from cell internalized AAV (left y axis, ^{111}In-^{125}I, solid bar) and radioactivity from total AAV (left y axis, ^{111}In, open bar) of AAV9 (left) and AAV-PHP.eB (right), at (A) 1 day post administration and (B) 3 days post administration. Embedded plot shows linear regression correlation between DNA concentration and internalized AAV quantification (red) or total AAV quantification (blue). The data are represented as the mean ± SD. $n = 4$ per time point. S. Intestine, small intestine; L. Intestine, large intestine; B. Marrows, bone marrows; W. Body Fat, white body fat.

(50 mg/mL, in 2 μL DMSO) was mixed with the AAV formulation at 4°C for 2 h. A centrifugal filter unit was used to remove unconjugated linkers and concentrate the AAV in 30 μL 0.2 M ammonium acetate buffer (pH 7.3). One mCi ^{111}In solution (BWXT Medical, Ottawa, Canada) was added to the AAV solution and incubated at 37°C, 300 rpm for 45 min, followed by adding 5 μL 0.05 M EDTA (pH 8) to chelate the unbound ^{111}In. Similar to ^{125}I labeling, the mixture was passed through a NAP-5 size-exclusion column to remove free ^{111}In and concentrated in ∼50 μL PBS.

The radiolabeling yield was calculated as the ratio of purified product radioactivity and starting radioactivity. The radiolabeled AAVs were quantified and characterized for physical and biological property before dosing the animals.

Size measurement

Apparent hydrodynamic sizes of radiolabeled AAVs were measured using a DynaPro NanoStar (Wyatt Technology, Santa Barbara, CA). AAVs were measured at ∼1×10^{13} vg/mL in PBS water at 25°C.

Intact and aggregation analysis

All radiolabeled materials were analyzed on an Agilent (Foster City, CA) HPLC system 1260II series with a Bio SEC-5 size-exclusion column, 5-μm particle size, 7.8 × 3,000 mm (SEC-HPLC), at an isocratic flow rate of 1.0 mL/min of PBS at pH 7.4 for 15 min. Radioactivity from the SEC-HPLC was detected by an in-line Raytest gamma detector (Elysia s.a., Angleur, Belgium). SEC-HPLC chromatogram profiles were used to quantify the intact and aggregated AAV after radiolabeling. Radiochemical purity after purification was determined by the peak area of radio-HPLC chromatographic data.

Mixtures of ^{125}I- and ^{111}In-labeled AAV were kept in PBS at room temperature for 72 h and analyzed by SEC-HPLC to examine the labeling stability.

Capsid analysis of AAVs

AAVs were analyzed by ProteinSimple Wes (Bio-Techne, Minneapolis, MN) by the default Wes sample preparation and assay conditions using the 12–230 kDa Wes Separation Module and the Anti-Mouse Detection Module. Anti-AAV VP1/VP2/VP3 mouse monoclonal antibodies (Progen, Wayne, PA) were used for immunoassay. Figures were quantified by ImageJ (version 1.53t) for protein relative quantification.

Genome and capsid titration

Genome titers were determined by Digital PCR (QuantStudio Absolute Q, Thermo Scientific) with TaqMan primer specific for the GFP transgene (Mr04329676_mr labeled with FAM-MGB, Thermo Scientific). Capsid titer was measured using AAV

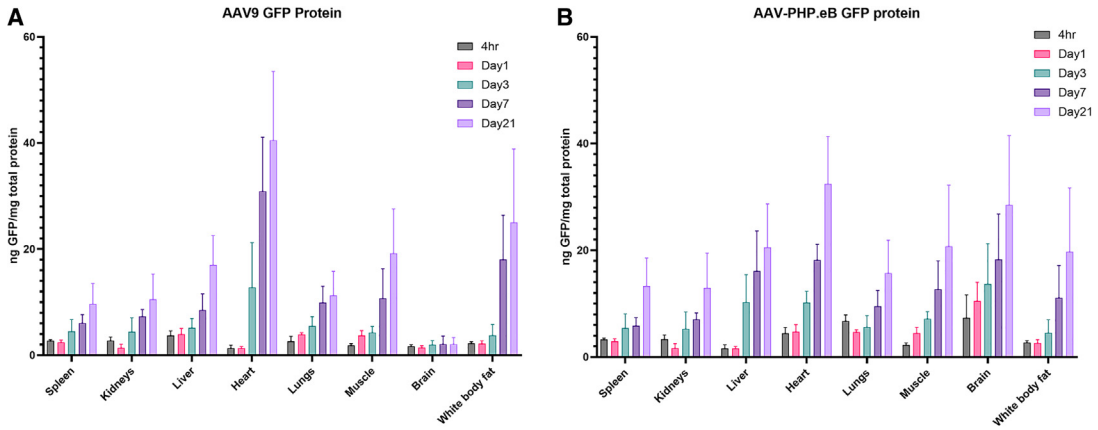

Figure 7. The tissue distribution of transgene product (GFP) after a single dose via i.v. administration in mice

(A) The GFP concentration (ng/mg total protein) in major organs and tissues from AAV9-treated mice up to 21 days post administration. (B) The GFP concentration (ng/mg total protein) in major organs and tissues from AAV-PHP.eB-treated mice up to 21 days post administration. The data are represented as the mean ± SD. $n = 4$ per time point. S. Intestine, small intestine; L. Intestine, large intestine; B. Marrows, bone marrows.

Xpress ELISA (Progen) following the manufacturer's protocol. Full/empty ratio was calculated by the result of genome and capsid titration.

Full / empty ratio = genome titer/capsid titer

Labeling efficiency

The radiolabeling efficiency was calculated based on capsid titration, product radioactivity, radiochemical purity, and the initial specific activity provided by the vendors. For example, 300 μCi were observed in a 500 μL ^{125}I-AAV9 solution (0.6 μCi/μL), and the viral titer was 9.0×10^{12} particles/mL. After decay correction, the specific activity of Na^{125}I in the reaction mixture is 17.4 Ci/mg. The total number of radioactive atoms in the product was calculated as $\frac{300\ \mu Ci}{17.4\ Ci/mg} \times \frac{6.023 \times 10^{23}\ /mol}{\times 147.89\ g/mol} = 11.21$, where 147.89 g/mol is the molecular weight of Na^{125}I and 6.023×10^{23}/mol is Avogadro constant. Thus, the mean number of ^{125}I atoms per virus particle in the preparation was 11.21.

In vitro transduction efficiency

To evaluate the potential effect of radiolabeling on AAV biological activity, HEK293T cells and HUVECs were transfected with AAV2-CMV-GFP and AAV9-CMV-GFP with and without label for transduction efficiency measurement. In brief, around 50,000 cells per well were plated into a 12-well plate. Immediately after plating, the ^{125}I-AAV, ^{111}In-AAV, and unlabeled AAV were incubated with cells at an MOI of from 100,000:1 to 1:1. At 48 h post treatment, GFP fluorescent microscopy images were acquired using a Zeiss Axiovert5 with a 488 nm excitation and a 508–601 nm filter. Next, cells were washed by ice-cold PBS and then trypsinized and suspended in PBS buffer at 4°C. For transduction efficiency analysis, the GFP-positive populations were measured using a Countess 3 FL Automated Cell Counter (Thermo Scientific) following the instrument handbook. For DNA quantification, DNeasy Blood & Tissue Kits (QIAGEN, Redwood City, CA) were used to extract the total DNA following the manufacturer's handbook. gDNA concentration was measured using NanoDrop Spectrophotometers (Thermo Scientific) and number of viral genomes determined by qPCR.

To investigate the capability of radiolabeling methods on different AAV serotypes, HEK293T cells and HUVECs were transfected with several AAV serotypes with and without label for transduction efficiency measurement. In brief, around 50,000 cells per well were plated into a 12-well plate. Immediately after plating, the ^{125}I AAV, ^{111}In AAV, and unlabeled AAV were incubated with cells at an MOI of 1,000:1. At 48 h post treatment, cells were trypsinized and suspended in PBS buffer at 4°C. GFP-positive populations were measured using a Countess 3 FL Automated Cell Counter (Thermo Scientific).

Cellular uptake analysis

HEK293T cells were seeded in a 12-well plate at 50,000 cells per well overnight. The day after, cells were transduced with ^{125}I/^{111}In-AAV2-CMV-GFP and ^{125}I/^{111}In-AAV2-Y444F-CMV-GFP at a multiplicity of 1,000 vg/cell in triplicate. For the anti-AAVR-treated group, anti-AAVR antibodies (ab105385, Abcam) were incubated with cells at concentration of 5 μg/mL in DMEM medium for 1 h prior to AAV transduction. At the designated time point, cells were trypsinized, washed in cold PBS three times, and suspended in PBS buffer to remove nonspecific binding AAVs. Collected cells were measured using a PerkinElmer Wizard2 analyzer (PerkinElmer, Billerica, MA), followed by DNA extraction and quantification using the method described above. After decay correction, the vector genome concentration was calculated based on specific activity.

Confocal fluorescence microscopy imaging

HEK293T cells were seeded in a 12-well glass-bottom plate (Cellvis, Mountain View, CA) at 50,000 cells per well overnight. The day

after, cells were transduced with ^{125}I/^{111}In-AAV2-CMV-GFP and ^{125}I/^{111}In-AAV2-Y444F-CMV-GFP at a multiplicity of 1,000 vg/cell in triplicate. For the anti-AAVR-treated group, anti-AAVR antibodies (ab105385, Abcam) were incubated with cells at a concentration of 5 μg/mL in DMEM medium for 1 h prior to AAV transduction. After 0, 2, 24, and 48 h, cells were washed in PBS twice, fixed with 4% paraformaldehyde in PBS, and permeabilized with 0.2% Triton X-100 for 10 min at room temperature. Permeabilized cells were blocked with PBS containing 10% goat serum (Abcam) and 3% fetal bovine serum (Thermo Scientific) for 1 h, incubated with anti-AAV2 mouse monoclonal antibody (Progen) only recognizing AAV2 intact capsids, and washed with PBS. Cells were then incubated with anti-mouse Alexa Fluor 555 secondary antibody (1:200 in blocking buffer), washed with PBS 3 times, and incubated with DraQ5 (1:1,000 in PBS) for nuclei staining (Thermo Scientific). Confocal fluorescence images were captured on Celldiscoverer 7 (Zeiss). Two separate signals are obtained: track 1 includes DraQ5 channels with a 640 nm excitation (0.2%, detector gain 650 V) and a 650–700 nm filter, and track 2 is an Alexa Fluor 555 channel with a 561 nm excitation (2.0%, detector gain 650 V) and a 400–650 nm filter.

Animal housing and procedure

All animal studies were performed in the Genentech animal facility, which was accredited by the Association for Assessment and Accreditation of Laboratory Animal Care International. All the protocols and procedures for animal studies were approved (approval no. 23-0590) by the Genentech Institutional Animal Care and Use Committee (IACUC) and performed in accordance with the institutional and regulatory guidelines. All the personnel involved in the animal experiments were trained according to IACUC guidelines.

Biodistribution of ^{125}I-AAV/^{111}In-AAVs

To demonstrate the capability of using the dual-isotope method in AAV biodistribution studies, ^{125}I/^{111}In-AAV9-CMV-GFP and ^{125}I/^{111}In-AAV-PHP.eb-CMV-GFP, as tool compounds, were evaluated in wild-type 6-week-old female C57BL/6 (The Jackson Laboratory, Bar Harbor, ME). In brief, 40 mice were divided into two groups (n = 20 each group). ^{125}I/^{111}In-AAV9 and ^{125}I/^{111}In-AAV-PHP.eb (1×10^{12} vg/mouse, 10 μCi/mouse) were administered via i.v. bolus, respectively. Blood and various tissues were collected at multiple intervals up to 21 days post-injection. Blood samples (50 μL) were collected from three mice in each dosing group at each time point and deposed into lithium heparin tubes and gently inverted several times to properly mix the anticoagulant. Tissue samples from different organs (e.g., the liver, spleen, heart, kidneys, lungs, brain, etc.) were collected from animals euthanized via exsanguination under anesthesia at the designated time points (n = 4). Collected tissues were washed with PBS buffer and stored at −80°C for future analysis. The radioactivity of individual isotopes of the whole tissue and blood was measured directly using a PerkinElmer Wizard2 gamma counter (Waltham, MA). Levels of ^{125}I and ^{111}In were quantified simultaneously under separate energy windows (15–85 keV for ^{125}I, 237–257 keV for ^{111}In). The readings were decay corrected to the time of dosing, and radioactivity data were calculated as a percentage of injected dose (%ID) normalized by volume/weight (%ID/mL or %ID/g).

Organs were fractioned and weighed to 20 mg pieces for further analysis. For DNA quantitation, organs and tissues were first dissociated using Tissue Dissociation Kits (Miltenyi Biotec, San Jose, CA). Total DNA was extracted from dissociated tissues using a MagMAX DNA Ultra Kit 2.0 (Thermo Scientific) followed by qPCR quantification targeting GFP transgene and mouse Tfrc as endogenous reference genes. GFP plasmid standard was directly purchased from Virovek and mouse gDNA quantification standard curve derived from a serial dilution of mouse genomic DNA (Promega, Madison, WI). RNA was extracted with a MagMAX mirVana Total RNA Isolation Kit (QIAGEN). cDNA was prepared using SuperScript IV VILO Master Mix (Thermo Scientific). RNA concentration was measured by NanoDrop and GFP cDNA concentrations were determined using the qPCR method mentioned above. GFP protein concentration and total protein concentration were analyzed using a GFP ELISA kit (Abcam, Cambridge, UK) and Pierce BCA Protein Assay Kits (Thermo Scientific). All of the analysis procedures above followed the manufacturer's instructions accordingly.

DATA AND CODE AVAILABILITY

The authors confirm that the data supporting the findings of this study are available within the article and its supplemental information.

ACKNOWLEDGMENTS

The authors would like to thank the In Vivo Study Group at Genentech for conducting all *in vivo* studies. All the work presented was financially supported by Genentech Inc.

AUTHOR CONTRIBUTIONS

Conceptualization, H.W., S.S., R.L., and B.-Q.S.; design, H.W., S.S., R.L., and B.-Q.S.; writing – original draft, H.W.; writing – review & editing, S.S., R.L., A.V.K., and B.-Q.S.; preparation of tables and figures, H.W.; supervision, S.S., R.L., A.V.K., and B.-Q.S. All authors read and approved the final manuscript.

DECLARATION OF INTERESTS

All authors are employees and stockholders of Genentech, Inc., and F. Hoffmann-La Roche Ltd.

DECLARATION OF GENERATIVE AI AND AI-ASSISTED TECHNOLOGIES IN THE WRITING PROCESS

During the preparation of this work the authors used GPT-4O in order to check spelling. After using this tool/service, the author(s) reviewed and edited the content as needed and take(s) full responsibility for the content of the publication.

SUPPLEMENTAL INFORMATION

Supplemental information can be found online at https://doi.org/10.1016/j.omtm.2024.101326.

REFERENCES

1. Atchison, R.W., Casto, B.C., and Hammon, W.M. (1965). Adenovirus-Associated Defective Virus Particles. Science *149*, 754–756. https://doi.org/10.1126/science.149.3685.754.

2. Mezzina, M., and Merten, O.W. (2011). Adeno-associated viruses. Methods Mol. Biol. *737*, 211–234. https://doi.org/10.1007/978-1-61779-095-9_9.

3. Stagg, S.M., Yoshioka, C., Davulcu, O., and Chapman, M.S. (2022). Cryo-electron Microscopy of Adeno-associated Virus. Chem. Rev. *122*, 14018–14054. https://doi.org/10.1021/acs.chemrev.1c00936.

4. Wang, D., Tai, P.W.L., and Gao, G. (2019). Adeno-associated virus vector as a platform for gene therapy delivery. Nat. Rev. Drug Discov. *18*, 358–378. https://doi.org/10.1038/s41573-019-0012-9.

5. Mietzsch, M., Jose, A., Chipman, P., Bhattacharya, N., Daneshparvar, N., McKenna, R., and Agbandje-McKenna, M. (2021). Completion of the AAV Structural Atlas: Serotype Capsid Structures Reveals Clade-Specific Features. Viruses *13*, 101. https://doi.org/10.3390/v13010101.

6. Gao, G., Vandenberghe, L.H., Alvira, M.R., Lu, Y., Calcedo, R., Zhou, X., and Wilson, J.M. (2004). Clades of Adeno-associated viruses are widely disseminated in human tissues. J. Virol. *78*, 6381–6388. https://doi.org/10.1128/JVI.78.12.6381-6388.2004.

7. Zincarelli, C., Soltys, S., Rengo, G., and Rabinowitz, J.E. (2008). Analysis of AAV serotypes 1-9 mediated gene expression and tropism in mice after systemic injection. Mol. Ther. *16*, 1073–1080. https://doi.org/10.1038/mt.2008.76.

8. Pillay, S., Zou, W., Cheng, F., Puschnik, A.S., Meyer, N.L., Ganaie, S.S., Deng, X., Wosen, J.E., Davulcu, O., Yan, Z., et al. (2017). Adeno-associated Virus (AAV) Serotypes Have Distinctive Interactions with Domains of the Cellular AAV Receptor. J. Virol. *91*, e00391-17. https://doi.org/10.1128/JVI.00391-17.

9. Wu, Z., Asokan, A., and Samulski, R.J. (2006). Adeno-associated virus serotypes: vector toolkit for human gene therapy. Mol. Ther. *14*, 316–327. https://doi.org/10.1016/j.ymthe.2006.05.009.

10. Naso, M.F., Tomkowicz, B., Perry, W.L., 3rd, and Strohl, W.R. (2017). Adeno-Associated Virus (AAV) as a Vector for Gene Therapy. BioDrugs *31*, 317–334. https://doi.org/10.1007/s40259-017-0234-5.

11. Choi, V.W., McCarty, D.M., and Samulski, R.J. (2006). Host cell DNA repair pathways in adeno-associated viral genome processing. J. Virol. *80*, 10346–10356. https://doi.org/10.1128/JVI.00841-06.

12. Issa, S.S., Shaimardanova, A.A., Solovyeva, V.V., and Rizvanov, A.A. (2023). Various AAV Serotypes and Their Applications in Gene Therapy: An Overview. Cells *12*, 785. https://doi.org/10.3390/cells12050785.

13. Gonin, P., and Gaillard, C. (2004). Gene transfer vector biodistribution: pivotal safety studies in clinical gene therapy development. Gene Ther. *11*, S98–S108. https://doi.org/10.1038/sj.gt.3302378.

14. Silva Lima, B., and Videira, M.A. (2018). Toxicology and Biodistribution: The Clinical Value of Animal Biodistribution Studies. Mol. Ther. Methods Clin. Dev. *8*, 183–197. https://doi.org/10.1016/j.omtm.2018.01.003.

15. Sun, K., and Liao, M.Z. (2022). Clinical Pharmacology Considerations on Recombinant Adeno-Associated Virus-Based Gene Therapy. J. Clin. Pharmacol. *62*, S79–S94. https://doi.org/10.1002/jcph.2141.

16. Li, C., and Samulski, R.J. (2020). Engineering adeno-associated virus vectors for gene therapy. Nat. Rev. Genet. *21*, 255–272. https://doi.org/10.1038/s41576-019-0205-4.

17. Chen, N., Sun, K., Chemuturi, N.V., Cho, H., and Xia, C.Q. (2022). The Perspective of DMPK on Recombinant Adeno-Associated Virus-Based Gene Therapy: Past Learning, Current Support, and Future Contribution. AAPS J. *24*, 31. https://doi.org/10.1208/s12248-021-00678-7.

18. Summerford, C., Johnson, J.S., and Samulski, R.J. (2016). AAVR: A Multi-Serotype Receptor for AAV. Mol. Ther. *24*, 663–666. https://doi.org/10.1038/mt.2016.49.

19. Berry, G.E., and Asokan, A. (2016). Cellular transduction mechanisms of adeno-associated viral vectors. Curr. Opin. Virol. *21*, 54–60. https://doi.org/10.1016/j.coviro.2016.08.001.

20. Agbandje-McKenna, M., and Kleinschmidt, J. (2011). AAV capsid structure and cell interactions. Methods Mol. Biol. *807*, 47–92. https://doi.org/10.1007/978-1-61779-370-7_3.

21. Chandran, J.S., Sharp, P.S., Karyka, E., Aves-Cruzeiro, J.M.d.C., Coldicott, I., Castelli, L., Hautbergue, G., Collins, M.O., and Azzouz, M. (2017). Site Specific Modification of Adeno-Associated Virus Enables Both Fluorescent Imaging of Viral Particles and Characterization of the Capsid Interactome. Sci. Rep. *7*, 14766. https://doi.org/10.1038/s41598-017-15255-2.

22. Bartlett, J.S., and Samulski, R.J. (1998). Fluorescent viral vectors: a new technique for the pharmacological analysis of gene therapy. Nat. Med. *4*, 635–637. https://doi.org/10.1038/nm0598-635.

23. Ballon, D.J., Rosenberg, J.B., Fung, E.K., Nikolopoulou, A., Kothari, P., De, B.P., He, B., Chen, A., Heier, L.A., Sondhi, D., et al. (2020). Quantitative Whole-Body Imaging of I-124-Labeled Adeno-Associated Viral Vector Biodistribution in Nonhuman Primates. Hum. Gene Ther. *31*, 1237–1259. https://doi.org/10.1089/hum.2020.116.

24. Yoon, S.Y., Gay-Antaki, C., Ponde, D.E., Poptani, H., Vite, C.H., and Wolfe, J.H. (2014). Quantitative, noninvasive, in vivo longitudinal monitoring of gene expression in the brain by co-AAV transduction with a PET reporter gene. Mol. Ther. Methods Clin. Dev. *1*, 14016. https://doi.org/10.1038/mtm.2014.16.

25. Seo, J.W., Ingham, E.S., Mahakian, L., Tumbale, S., Wu, B., Aghevlian, S., Shams, S., Baikoghli, M., Jain, P., Ding, X., et al. (2020). Positron emission tomography imaging of novel AAV capsids maps rapid brain accumulation. Nat. Commun. *11*, 2102. https://doi.org/10.1038/s41467-020-15818-4.

26. Zhao, J., Yue, Y., Patel, A., Wasala, L., Karp, J.F., Zhang, K., Duan, D., and Lai, Y. (2020). High-Resolution Histological Landscape of AAV DNA Distribution in Cellular Compartments and Tissues following Local and Systemic Injection. Mol. Ther. Methods Clin. Dev. *18*, 856–868. https://doi.org/10.1016/j.omtm.2020.08.006.

27. Devous, M.D., Sr., Lowe, J.L., and Payne, J.K. (1992). Dual-isotope brain SPECT imaging with technetium-99m and iodine-123: validation by phantom studies. J. Nucl. Med. *33*, 2030–2035.

28. Rafidi, H., Estevez, A., Ferl, G.Z., Mandikian, D., Stainton, S., Sermeño, L., Williams, S.P., Kamath, A.V., Koerber, J.T., and Boswell, C.A. (2021). Imaging Reveals Importance of Shape and Flexibility for Glomerular Filtration of Biologics. Mol. Cancer Therapeut. *20*, 2008–2015. https://doi.org/10.1158/1535-7163.MCT-21-0116.

29. Yip, V., Lee, M.V., Saad, O.M., Ma, S., Khojasteh, S.C., and Shen, B.Q. (2021). Preclinical Characterization of the Distribution, Catabolism, and Elimination of a Polatuzumab Vedotin-Piiq (POLIVY((R))) Antibody-Drug Conjugate in Sprague Dawley Rats. J. Clin. Med. *10*, 1323. https://doi.org/10.3390/jcm10061323.

30. Carney, P.L., Rogers, P.E., and Johnson, D.K. (1989). Dual isotope study of iodine-125 and indium-111-labeled antibody in athymic mice. J. Nucl. Med. *30*, 374–384.

31. Millar, W.T., and Smith, J.F. (1983). Protein iodination using Iodogen. Int. J. Appl. Radiat. Isot. *34*, 639–641. https://doi.org/10.1016/0020-708x(83)90068-6.

32. Banks, P.R., and Paquette, D.M. (1995). Comparison of three common amine reactive fluorescent probes used for conjugation to biomolecules by capillary zone electrophoresis. Bioconjugate Chem. *6*, 447–458. https://doi.org/10.1021/bc00034a015.

33. Ellis, B.L., Hirsch, M.L., Barker, J.C., Connelly, J.P., Steininger, R.J., 3rd, and Porteus, M.H. (2013). A survey of ex vivo/in vitro transduction efficiency of mammalian primary cells and cell lines with Nine natural adeno-associated virus (AAV1-9) and one engineered adeno-associated virus serotype. Virol. J. *10*, 74. https://doi.org/10.1186/1743-422X-10-74.

34. Huang, Q., Chan, K.Y., Tobey, I.G., Chan, Y.A., Poterba, T., Boutros, C.L., Balazs, A.B., Daneman, R., Bloom, J.M., Seed, C., and Deverman, B.E. (2019). Delivering genes across the blood-brain barrier: LY6A, a novel cellular receptor for AAV-PHP.B capsids. PLoS One *14*, e0225206. https://doi.org/10.1371/journal.pone.0225206.

35. Rafidi, H., Rajan, S., Urban, K., Shatz-Binder, W., Hui, K., Ferl, G.Z., Kamath, A.V., and Boswell, C.A. (2022). Effect of molecular size on interstitial pharmacokinetics and tissue catabolism of antibodies. mAbs *14*, 2085535. https://doi.org/10.1080/19420862.2022.2085535.

36. Weinmann, J., Weis, S., Sippel, J., Tulalamba, W., Remes, A., El Andari, J., Herrmann, A.K., Pham, Q.H., Borowski, C., Hille, S., et al. (2020). Identification of a myotropic AAV by massively parallel in vivo evaluation of barcoded capsid variants. Nat. Commun. *11*, 5432. https://doi.org/10.1038/s41467-020-19230-w.

37. Kelich, J.M., Ma, J., Dong, B., Wang, Q., Chin, M., Magura, C.M., Xiao, W., and Yang, W. (2015). Super-resolution imaging of nuclear import of adeno-associated virus in live cells. Mol. Ther. Methods Clin. Dev. *2*, 15047. https://doi.org/10.1038/mtm.2015.47.

38. Golm, S.K., Hubner, W., and Muller, K.M. (2023). Fluorescence Microscopy in Adeno-Associated Virus Research. Viruses *15*, 1174. https://doi.org/10.3390/v15051174.

39. Bartlett, J.S., Wilcher, R., and Samulski, R.J. (2000). Infectious entry pathway of adeno-associated virus and adeno-associated virus vectors. J. Virol. *74*, 2777–2785. https://doi.org/10.1128/jvi.74.6.2777-2785.2000.

40. Xiao, P.J., Li, C., Neumann, A., and Samulski, R.J. (2012). Quantitative 3D tracing of gene-delivery viral vectors in human cells and animal tissues. Mol. Ther. *20*, 317–328. https://doi.org/10.1038/mt.2011.250.

41. Zhang, C., Zhou, X., Yao, T., Tian, Z., and Zhou, D. (2018). Precision Fluorescent Labeling of an Adeno-Associated Virus Vector to Monitor the Viral Infection Pathway. Biotechnol. J. *13*, e1700374. https://doi.org/10.1002/biot.201700374.

42. Kothari, P., De, B.P., He, B., Chen, A., Chiuchiolo, M.J., Kim, D., Nikolopoulou, A., Amor-Coarasa, A., Dyke, J.P., Voss, H.U., et al. (2017). Radioiodinated Capsids Facilitate In Vivo Non-Invasive Tracking of Adeno-Associated Gene Transfer Vectors. Sci. Rep. *7*, 39594. https://doi.org/10.1038/srep39594.

43. Zhong, L., Li, B., Mah, C.S., Govindasamy, L., Agbandje-McKenna, M., Cooper, M., Herzog, R.W., Zolotukhin, I., Warrington, K.H., Jr., Weigel-Van Aken, K.A., et al. (2008). Next generation of adeno-associated virus 2 vectors: point mutations in tyrosines lead to high-efficiency transduction at lower doses. Proc. Natl. Acad. Sci. USA *105*, 7827–7832. https://doi.org/10.1073/pnas.0802866105.

44. Petrs-Silva, H., Dinculescu, A., Li, Q., Min, S.H., Chiodo, V., Pang, J.J., Zhong, L., Zolotukhin, S., Srivastava, A., Lewin, A.S., and Hauswirth, W.W. (2009). High-efficiency transduction of the mouse retina by tyrosine-mutant AAV serotype vectors. Mol. Ther. *17*, 463–471. https://doi.org/10.1038/mt.2008.269.

45. Pillay, S., Meyer, N.L., Puschnik, A.S., Davulcu, O., Diep, J., Ishikawa, Y., Jae, L.T., Wosen, J.E., Nagamine, C.M., Chapman, M.S., and Carette, J.E. (2016). An essential receptor for adeno-associated virus infection. Nature *530*, 108–112. https://doi.org/10.1038/nature16465.

46. Zhang, R., Cao, L., Cui, M., Sun, Z., Hu, M., Zhang, R., Stuart, W., Zhao, X., Yang, Z., Li, X., et al. (2019). Adeno-associated virus 2 bound to its cellular receptor AAVR. Nat. Microbiol. *4*, 675–682. https://doi.org/10.1038/s41564-018-0356-7.

47. Liguore, W.A., Domire, J.S., Button, D., Wang, Y., Dufour, B.D., Srinivasan, S., and McBride, J.L. (2019). AAV-PHP.B Administration Results in a Differential Pattern of CNS Biodistribution in Non-human Primates Compared with Mice. Mol. Ther. *27*, 2018–2037. https://doi.org/10.1016/j.ymthe.2019.07.017.